Acta Crystallographica Section B
Structural Science
ISSN 0108-7681

Structure of the clinopyroxene-type compound $CaCuGe_2O_6$ between 15 and 800 K

Günther J. Redhammer,[a,b]* Gerold Tippelt,[b] Michael Merz,[a] Georg Roth,[a] Werner Treutmann[c] and Georg Amthauer[b]

[a]Institute of Crystallography, University of Technology Aachen, Jägerstrasse 17/19, D-52056 Aachen, Germany, [b]Division Mineralogy and Material Science, Department of Geography, Geology and Mineralogy, University of Salzburg, Hellbrunnerstrasse 34, A-5020 Salzburg, Austria, and [c]Institute of Mineralogy, University of Marburg/Lahn, Hans-Meerwein-strasse, D-40000 Marburg/Lahn, Germany

Correspondence e-mail: guenther.redhammer@aon.at

Received 20 September 2004
Accepted 27 April 2005

$CaCuGe_2O_6$ shows a strongly distorted clinopyroxene-type structure with $P2_1/c$ symmetry at 298 K. The Cu^{2+} ion at the $M1$ site is coordinated by six O atoms forming an octahedron, which deviates significantly from ideal geometry. Individual $M1$ sites are connected *via* common edges to form an infinite zigzag chain parallel to the crystallographic c axis. The Ca^{2+} ion at $M2$ shows a sevenfold coordination. $M2$ sites are connected to the $M1$ chain *via* three common edges, thereby forming a metal layer within the bc plane. Besides the strong Jahn–Teller distortion of the Cu site, the structure of the title compound differs from 'normal' clinopyroxenes by a distortion of alternate layers of Ge sites. While the Ge(A) site is fourfold coordinated by O atoms, forming infinite chains of corner-sharing chains parallel to the c axis, the Ge(B) site exhibits a fivefold coordination, thereby forming a true two-dimensional layer of edge-sharing GeO_5 bipyramids. Decreasing the temperature causes a magnetic phase transition at 40 K, as monitored by a broad maximum in the magnetic susceptibility and by discontinuities in the lattice parameters. Increasing the temperature causes variations in bond lengths, edge lengths and bond angles. Most prominent is the increase of one bond length of the Ge(B) site and the increase of the tetrahedral bridging angle of the Ge(A) site. At 660 K a crystallographic phase transition is observed where the symmetry changes from $P2_1/c$ to $C2/c$. The transition is accompanied by large changes in the lattice parameters which are indicative of distinct topological changes of several structural building units. The high-temperature $C2/c$ structure is similar to that of the germanate clinopyroxene $CaMgGe_2O_6$.

1. Introduction

Clinopyroxenes, a mineral group occurring in abundance in nature and containing a variety of rock-forming minerals, have gained substantial interest in solid-state science because of the distinct low-dimensional character of their structure (quasi-one-dimensional). Within this group, several compounds have been discovered that show spin-gap behaviour, among them $LiTi^{3+}Si_2O_6$ and $NaTiSi_2O_6$ (Isobe *et al.*, 2002; Redhammer *et al.*, 2003), $LiVGe_2O_6$ (Gavilano *et al.*, 2000; Lumdsen *et al.*, 2000; Vonlanthen *et al.*, 2002) and $CaCuGe_2O_6$ (Sasago *et al.*, 1995; Zheludev *et al.*, 1996; Valenti *et al.*, 2002). Susceptibility measurements of Sasago *et al.* (1995) on $CaCuGe_2O_6$ have shown the existence of a spin-singlet ground state. It was stated that the spin gap is intrinsic and that there is no (magnetic) phase transition between 5 and 300 K. Zheludev *et al.* (1996) found that despite the distinct structural low dimensionality of the arrangement of magnetic sites in the compound, the experimental data (inelastic neutron scat-

© 2005 International Union of Crystallography
Printed in Great Britain – all rights reserved

tering) can be described by an ensemble of weakly interacting antiferromagnetic dimers, which are composed of pairs of Cu^{2+} ions (Zheludev *et al.*, 1996). Recently, Valenti *et al.* (2002) demonstrated, by means of *ab initio* electronic structure analysis and quantum Monte-Carlo calculations, that longer-range magnetic interactions dominate over short-range interactions. The spin-singlet behaviour in $CaCuGe_2O_6$ is induced by third nearest-neighbour Cu^{2+} pairs, *i.e.* by Cu^{2+} atoms of two different neighbouring Cu^{2+} chains (intra-chain interaction), but not by Cu^{2+} pairs within the Cu^{2+} chain. The almost complete cancellation of the nearest and next-nearest neighbour interactions make the magnetic properties of these compounds very susceptible to even small distortions of the crystal structure. This clearly calls for a thorough structure analysis of these compounds at high and low temperatures.

The title compound exhibits a strongly distorted clinopyroxene-type structure, which was first described by Behruzi *et al.* (1986). At room temperature (298 K) it shows $P2_1/c$ symmetry, which is rare for calcium clinopyroxenes (mostly $C2/c$ symmetry), but typical for the low-temperature (LT) form of *e.g.* the lithium clinopyroxenes (Redhammer & Roth, 2004*a*,*b*). Behruzi *et al.* (1986) were also the first to notice the presence of a phase transition in $CaCuGe_2O_6$ at elevated temperature, but only lattice parameters and space-group symmetry ($P2_1/n$) were determined for this high-temperature (HT) form. Tovar & Eysel (1999) concluded from X-ray powder diffraction data that the high-temperature phase has $C2/c$ symmetry. This was independently confirmed by Redhammer (2001), again using X-ray powder diffraction data. No single-crystal structure data have been available for $CaCuGe_2O_6$ for temperatures other than 298 K until now. Structural data for low temperatures have been extrapolated from the 298 K data. Motivated by the success in synthesizing single crystals of $CaCuGe_2O_6$, the present work aims towards:

(i) studying the evolution of lattice parameters as a function of temperature over a wide temperature range,

(ii) presenting the evolution of structural and distortional parameters as a function of temperature,

(iii) determining the symmetry of the high-temperature phase and

(iv) studying the topological differences between the $P2_1/c$ low-temperature form, the high-temperature form and the less distorted germanate clinopyroxene, $CaMgGe_2O_6$ (Redhammer, 2001).

2. Experimental

2.1. Material synthesis

Single crystals of the title compound were obtained using ceramic sintering techniques. A stoichiometric mixture of $CaCO_3$, CuO and GeO_2 was carefully ground under ethanol, pressed into pellets, placed into an open platinum crucible and fired under ambient pressure and oxygen fugacity in the temperature range 1173–1373 K. After a heating cycle of 5 d of sintering time, the sample material was reground, pressed and reheated. $CuGeO_3$ was observed as an impurity phase in the product of the first two runs. This procedure was repeated eight times, after which a single-phase product of $CaCuGe_2O_6$ was obtained. In a final synthesis cycle, part of the sample was fired at 1423 K for 6 h which resulted in a coarse-grained single-phase product of $CaCuGe_2O_6$, which contained single crystals suitable for single-crystal X-ray diffraction experiments.

2.2. Powder X-ray diffraction

To obtain detailed information on the temperature variation of the lattice parameters, step-scan X-ray powder diffraction measurements (10–110° in 2Θ, continuous scan) were carried out in the temperature range 15–873 K. Low-temperature data (15–298 K) were collected at the Institute of Crystallography, RWTH Aachen, on a Philips X'Pert diffractometer equipped with a Janis CCS-250 cryostat and with parallel beam optics [Cu $K\alpha_1$ radiation, primary side: X-ray mirror combined with 2 bounce Ge(222) monochromator, primary and secondary side 0.04 rad soller slits; secondary optics: parabolic X-ray mirror which focused the parallel beam on a proportional counter]. High-temperature data were collected at the University of Salzburg on a Philips X'Pert diffractometer system, equipped with an Anton PAAR HTK-16 high-temperature chamber (Cu $K\alpha_{1,2}$ radiation, primary and secondary side 0.04 rad soller slits, secondary side graphite monochromator). Lattice parameters were obtained by whole pattern fitting using the LeBail method, as implemented in the *FULLPROF* program (Rodriguez-Carvajal, 2001).

2.3. Single-crystal X-ray diffraction

A turquoise–blue crystal of $CaCuGe_2O_6$ (dimensions $0.14 \times 0.13 \times 0.10$ mm^3, formula weight $M_r = 344.80$ g mol^{-1}, absorption coefficient $\mu = 18.269$ mm^{-1} for Mo $K\alpha$) was used in single-crystal X-ray diffraction experiments. Intensity data sets at 100, 150, 200, 250 and 298 K, respectively, were collected on a Stoe IPDS II imaging-plate diffractometer system (Mo $K\alpha$ radiation, pyrolytic graphite monochromator), equipped with a cryo-stream liquid N_2 cryostat (85–300 K, accuracy at least 1 K). Data sets were collected up to 65.0° in 2θ within an ω range of 0–180° and two different φ positions in most cases; the ω rotation during exposure was 2.0° per frame. The high-temperature experiments (328, 361, 470, 570, 612, 629, 646, 654, 717, 729, 763 and 796 K, respectively, accuracy at least 3 K) were collected on a Stoe IPDS I image-plate diffractometer system, equipped with a heating device built in-house. The same crystal as for the low-temperature measurements was used. Here, data sets were collected up to 56.0° in 2θ. Owing to the geometry of the heating device, only a limited ω range of 60–210° was accessible. Data were measured from low to high temperatures. Attempts to re-measure data at lower T after the data collection at 796 K failed as the crystal disintegrated upon cooling when passing through the phase transition a second time. Lattice parameters determined from single-crystal X-ray diffraction data agree

Table 1
Experimental details of $CaCuGe_2O_6$ at selected temperatures.

Full data can be obtained from the CIF, which has been deposited.

	100 K	200 K	RT
Crystal data			
Chemical formula	$CaCuGe_2O_6$	$CaCuGe_2O_6$	$CaCuGe_2O_6$
M_r	344.8	344.8	344.8
Cell setting, space group	Monoclinic, $P2_1/c$	Monoclinic, $P2_1/c$	Monoclinic, $P2_1/c$
a, b, c (Å)	10.1798 (12), 9.1869 (7), 5.1978 (6)	10.1853 (12), 9.1959 (7), 5.2013 (6)	10.1930 (12), 9.2039 (7), 5.2078 (6)
β (°)	105.614 (12)	105.649 (12)	105.688 (12)
V (Å^3)	468.16 (9)	469.11 (9)	470.37 (9)
Z	4	4	4
D_x (Mg m^{-3})	4.892	4.882	4.869
Radiation type	Mo $K\alpha$	Mo $K\alpha$	Mo $K\alpha$
No. of reflections for cell parameters	6685	6540	6631
θ range (°)	2.2–32.1	2.1–32.1	2.2–32.1
μ (mm^{-1})	18.22	18.22	18.22
Temperature (K)	100 (1)	200 (1)	298 (1)
Crystal form, colour	Cuboid, pale green	Cuboid, pale green	Cuboid, pale green
Crystal size (mm)	0.14 × 0.13 × 0.10	0.14 × 0.13 × 0.10	0.14 × 0.13 × 0.10
Data collection			
Diffractometer	Stoe IPDS 2	Stoe IPDS 2	Stoe IPDS 2
Data collection method	Rotation method	Rotation method	Rotation method
Absorption correction	Empirical (using intensity measurements)	Empirical (using intensity measurements)	Empirical (using intensity measurements)
T_{min}	0.097	0.084	0.093
T_{max}	0.150	0.162	0.158
No. of measured, independent and observed reflections	5815, 1616, 1415	5828, 1626, 1415	5565, 1622, 1438
Criterion for observed reflections	$I > 2\sigma(I)$	$I > 2\sigma(I)$	$I > 2\sigma(I)$
R_{int}	0.039	0.037	0.038
θ_{max} (°)	32.2	32.2	32.2
Range of h, k, l	$-15 \Rightarrow h \Rightarrow 15$ $-13 \Rightarrow k \Rightarrow 13$ $-7 \Rightarrow l \Rightarrow 7$	$-15 \Rightarrow h \Rightarrow 15$ $-13 \Rightarrow k \Rightarrow 13$ $-7 \Rightarrow l \Rightarrow 7$	$-15 \Rightarrow h \Rightarrow 15$ $-13 \Rightarrow k \Rightarrow 13$ $-7 \Rightarrow l \Rightarrow 7$
Refinement			
Refinement on	F^2	F^2	F^2
$R[F^2 > 2\sigma(F^2)]$, $wR(F^2)$, S	0.025, 0.056, 1.06	0.025, 0.052, 1.07	0.030, 0.063, 1.1
No. of reflections	1616	1626	1622
No. of parameters	92	92	92
H-atom treatment	No H atoms present	No H atoms present	No H atoms present
Weighting scheme	$w = 1/[\sigma^2(F_o^2) + (0.0229P)^2 + 1.6631P]$, where $P = (F_o^2 + 2F_c^2)/3$	$w = 1/[\sigma^2(F_o^2) + (0.0163P)^2 + 1.812P]$, where $P = (F_o^2 + 2F_c^2)/3$	$w = 1/[\sigma^2(F_o^2) + (0.0237P)^2 + 1.7862P]$, where $P = (F_o^2 + 2F_c^2)/3$
$(\Delta/\sigma)_{max}$	<0.0001	0.001	<0.0001
$\Delta\rho_{max}$, $\Delta\rho_{min}$ (e Å^{-3})	0.80, −0.91	0.75, −0.81	0.85, −0.85
Extinction method	*SHELXL*	*SHELXL*	*SHELXL*
Extinction coefficient	0.0091 (6)	0.0097 (5)	0.0108 (6)

	420 K	525 K	630 K
Crystal data			
Chemical formula	$CaCuGe_2O_6$	$CaCuGe_2O_6$	$CaCuGe_2O_6$
M_r	344.8	344.8	344.8
Cell setting, space group	Monoclinic, $P2_1/c$	Monoclinic, $C2/c$	Monoclinic, $C2/c$
a, b, c (Å)	10.2165 (12), 9.2483 (7), 5.2429 (6)	10.2453 (12), 9.2118 (9), 5.4115 (7)	10.2448 (12), 9.1898 (9), 5.4023 (7)
β (°)	105.942 (12)	106.931 (14)	107.090 (14)
V (Å^3)	476.32 (9)	488.50 (10)	486.16 (10)
Z	4	4	4
D_x (Mg m^{-3})	4.808	4.688	4.711
Radiation type	Mo $K\alpha$	Mo $K\alpha$	Mo $K\alpha$
No. of reflections for cell parameters	3292	1683	1823
θ range (°)	2.1–27.7	3.0–27.8	2.2–28.0
μ (mm^{-1})	18.22	17.54	17.63
Temperature (K)	629 (2)	712 (2)	796 (2)
Crystal form, colour	Cuboid, pale green	Cuboid, pale green	Cuboid, pale green
Crystal size (mm)	0.14 × 0.13 × 0.10	0.14 × 0.13 × 0.10	0.14 × 0.13 × 0.10
Data collection			
Diffractometer	Stoe IPDS 1	Stoe IPDS 1	Stoe IPDS 1
Data collection method	Rotation method	Rotation method	Rotation method

Table 1 (continued)

	420 K	525 K	630 K
Absorption correction	Empirical (using intensity measurements)	Empirical (using intensity measurements)	Empirical (using intensity measurements)
T_{min}	0.094	0.102	0.102
T_{max}	0.158	0.172	0.172
No. of measured, independent and observed reflections	5005, 1053, 778	1629, 510, 392	1633, 493, 407
Criterion for observed reflections	$I > 2\sigma(I)$	$I > 2\sigma(I)$	$I > 2\sigma(I)$
R_{int}	0.060	0.048	0.034
θ_{max} (°)	27.9	27.8	28.0
Range of h, k, l	$-13 \Rightarrow h \Rightarrow 13$ $-12 \Rightarrow k \Rightarrow 12$ $-6 \Rightarrow l \Rightarrow 6$	$-13 \Rightarrow h \Rightarrow 13$ $-11 \Rightarrow k \Rightarrow 12$ $-6 \Rightarrow l \Rightarrow 6$	$-13 \Rightarrow h \Rightarrow 13$ $-12 \Rightarrow k \Rightarrow 12$ $-6 \Rightarrow l \Rightarrow 6$
Refinement			
Refinement on	F^2	F^2	F^2
$R[F^2 > 2\sigma(F^2)]$, $wR(F^2)$, S	0.047, 0.085, 1.16	0.034, 0.085, 1.05	0.031, 0.059, 1.07
No. of reflections	1053	510	493
No. of parameters	92	48	48
H-atom treatment	No H atoms present	No H atoms present	No H atoms present
Weighting scheme	$w = 1/[\sigma^2(F_o^2) + (0.0265P)^2 + 3.3784P]$, where $P = (F_o^2 + 2F_c^2)/3$	$w = 1/[\sigma^2(F_o^2) + (0.0471P)^2]$, where $P = (F_o^2 + 2F_c^2)/3$	$w = 1/[\sigma^2(F_o^2) + (0.028P)^2]$, where $P = (F_o^2 + 2F_c^2)/3$
$(\Delta/\sigma)_{max}$	<0.0001	<0.0001	<0.0001
$\Delta\rho_{max}$, $\Delta\rho_{min}$ (e Å^{-3})	0.97, −0.96	0.80, −0.75	0.63, −0.58
Extinction method	*SHELXL*	*SHELXL*	*SHELXL*
Extinction coefficient	0.0055 (6)	0.0057 (7)	0.0063 (5)

Computer programs used: *Stoe X-Area* (Stoe & Cie, 2002), *SHELXS*97 (Sheldrick, 1997*a*), *SHELXL*97 (Sheldrick, 1997*b*), *DIAMOND* (Brandenburg & Berndt, 1999), *WinGX*51.64.0 (Farrugia, 1999). † Footnote: T_{min} and T_{max} are the result of an individual shape optimization for each temperature.

well with those determined from powder X-ray diffraction. An absorption correction was carried out empirically *via* symmetry equivalents using *SHAPE* software (Stoe & Cie, 1996). Structure solution (using Patterson methods) and the subsequent refinement were carried out with the programs *SHELXS*97 (Sheldrick, 1997*a*) and *SHELXL*97 (Sheldrick, 1997*b*), as implemented in the program suite *WinGX*1.64 (Farrugia, 1999). X-ray scattering factors in their ionic form, together with anomalous dispersion coefficients, were taken from the *International Tables for Crystallography* (Wilson, 1992).

2.4. SQUID magnetometry

The magnetic measurements were performed at the University of Marburg/Lahn on a MPMS-2 SQUID magnetometer (Quantum Design, San Diego, USA). A small amount (35.3 mg) of $CaCuGe_2O_6$ was placed into small KLF containers and brought into a measuring position using a straw. The variation of the magnetization as a function of temperature at fixed external magnetic fields was studied.

3. Results and discussion

The intensity data set, collected at 298 K, was used to build up the structural model for the title compound. Indexing of the data and the analysis of systematic absences supported the assignment of the space group $P2_1/c$. Structure solution using Patterson methods and subsequent structure refinement yields a model with one symmetrically independent Ca^{2+}, one Cu^{2+}, two Ge^{4+} and six O^{2-} positions, respectively. The model is in close agreement with the structure given by Behruzi *et al.* (1986). Full anisotropic refinements of all non-symmetry equivalent atoms resulted in final agreement values of R_1 = 0.038 and wR_2 = 0.063 (all data) with residual electron densities below 0.9 e Å^{-3}. Table 1 contains the crystal data, and details on data collection and structure refinements for $CaCuGe_2O_6$ for five selected temperatures. Table 2 displays selected geometrical and distortional parameters for the temperatures given in Table 1.[1] A compilation of all the lattice parameters of $CaCuGe_2O_6$ in the temperature range 15–873 K can be obtained from the first author upon request.

In the following section, the crystal structure of $CaCuGe_2O_6$ at 298 K will be compared with $CaMgGe_2O_6$, a germanate compound which also reveals the clinopyroxene-type structure (Redhammer, 2001). $CaMgGe_2O_6$ was chosen for comparison with $CaCuGe_2O_6$ as the ionic radius of Mg^{2+} in octahedral coordination is quite similar to that of sixfold coordinated Cu^{2+} (0.72 and 0.73 Å; Shannon & Prewitt, 1969). Contrary to the title compound, the Mg^{2+} analogue has $C2/c$ symmetry at room temperature; a = 10.1064 (7), b = 8.9855 (6), c = 5.4323 (4) Å, β = 105.31 (1)°, Z = 4. The structure of $CaMgGe_2O_6$ (and of the clinopyroxenes in general) is built up by three main building units: zigzag chains of edge-sharing $M1$ sites hosting the Mg^{2+} cation in a regular octahedral coordination, zigzag chains of edge-sharing $M2$ sites, hosting Ca^{2+}, which shows a 4 + 4-fold coordination and corner-shared chains of slightly kinked GeO_4 tetrahedra, all running parallel

[1] Supplementary data for this paper are available from the IUCr electronic archives (Reference: WS5021). Services for accessing these data are described at the back of the journal.

Table 2
Selected bond lengths (Å), bond angles (°) and polyhedral distortion parameters for $CaCuGe_2O_6$ at different temperatures (full data are available online *via* the CIF).

T (K)	100	200	298	629	717	796
Ca—O1*A*	2.432 (3)	2.438 (2)	2.441 (3)	2.456 (4)	2.405 (6)	2.407 (5)
Ca—O1*B*	2.445 (2)	2.444 (2)	2.450 (3)	2.467 (4)	2.405 (6)	2.407 (5)
Ca—O2*A*	2.332 (2)	2.332 (2)	2.334 (3)	2.331 (4)	2.363 (6)	2.358 (5)
Ca—O2*B*	2.512 (2)	2.510 (2)	2.517 (3)	2.530 (3)	2.363 (6)	2.358 (5)
Ca—O3*A*	2.465 (2)	2.466 (2)	2.475 (3)	2.503 (3)	2.712 (6)	2.701 (5)
Ca—O3*B*	2.612 (2)	2.621 (2)	2.627 (3)	2.650 (3)	2.712 (6)	2.701 (5)
Ca—O3*B*	2.473 (2)	2.472 (2)	2.475 (3)	2.496 (3)	2.705 (6)	2.706 (5)
⟨Ca—O⟩	2.467	2.469	2.474	2.491	2.546	2.543
BLD_{M2}	2.25	2.26	2.28	2.51	6.40	6.30
$Vol._{M2}$	21.69	21.74	21.89	22.38	27.40	27.31
Cu—O1*A*	2.284 (2)	2.288 (2)	2.293 (3)	2.312 (3)	2.253 (6)	2.244 (5)
Cu—O1*A*	1.940 (2)	1.941 (2)	1.939 (3)	1.944 (3)	1.987 (6)	1.973 (5)
Cu—O1*B*	2.093 (2)	2.095 (2)	2.104 (3)	2.121 (3)	2.253 (6)	2.244 (5)
Cu—O1*B*	1.950 (2)	1.950 (2)	1.949 (3)	1.943 (3)	1.987 (6)	1.973 (5)
Cu—O2*A*	1.969 (2)	1.972 (2)	1.968 (3)	1.979 (3)	2.109 (6)	2.129 (5)
Cu—O2*B*	2.443 (2)	2.444 (2)	2.443 (3)	2.434 (3)	2.109 (6)	2.129 (5)
⟨Cu—O⟩	2.113	2.115	2.116	2.122	2.116	2.115
⟨O—O⟩	2.980	2.983	2.985	2.997	2.993	2.985
BLD	7.90	7.91	7.94	7.88	4.29	4.48
ELD	8.41	8.37	8.35	8.08	5.41	5.32
OAV	97.69	95.73	95.98	83.99	40.74	40.35
Vol.	11.92	11.96	11.98	12.14	12.37	12.29
Cu—Cu—1NN†	3.062	3.067	3.072	3.103	3.199	3.205
Cu—Cu—3NN	6.206	6.207	6.208	6.177	5.799	5.805
Ge(*A*)—O1*A*	1.7351 (2)	1.731 (2)	1.733 (3)	1.727 (3)	1.732 (6)	1.731 (5)
Ge(*A*)—O2*A*	1.710 (2)	1.708 (2)	1.708 (3)	1.711 (3)	1.722 (6)	1.717 (5)
Ge(*A*)—O3*A*	1.790 (2)	1.788 (2)	1.783 (3)	1.781 (3)	1.774 (6)	1.775 (5)
Ge(*A*)—O3*A*	1.783 (2)	1.789 (2)	1.790 (3)	1.799 (3)	1.816 (6)	1.809 (5)
⟨Ge(*A*)—O⟩	1.755	1.754	1.754	1.754	1.761	1.758
BLD	1.83	1.97	1.89	2.02	1.93	1.94
ELD	1.98	1.90	1.98	1.86	2.71	2.80
TAV	38.23	38.45	38.29	36.44	46.96	48.39
$Vol._{Ge(A)}$	2.74	2.73	2.73	2.74	2.76	2.74
Bridging angle	136.5 (1)	136.8 (1)	137.6 (1)	139.3 (1)	159.4 (1)	160.4 (1)
τ	112.91 (9)	112.92 (8)	112.91 (9)	112.93 (9)	114.29 (9)	114.33 (9)
Ge(*B*)—O1*B*	1.767 (2)	1.770 (2)	1.764 (3)	1.753 (3)	–	–
Ge(*B*)—O2*B*	1.774 (2)	1.775 (2)	1.772 (3)	1.745 (3)	–	–
Ge(*B*)—O2*B*	2.055 (2)	2.069 (2)	2.080 (3)	2.195 (3)	–	–
Ge(*B*)—O3*B*	1.776 (2)	1.776 (2)	1.774 (3)	1.768 (3)	–	–
Ge(*B*)—O3*B*	1.892 (2)	1.893 (2)	1.892 (3)	1.882 (3)	–	–
⟨Ge(*B*)—O⟩	1.853	1.857	1.856	1.868	–	–
⟨O—O⟩	2.785	2.790		2.797	–	–
BLD	5.21	5.35	5.59	7.28	–	–
ELD	6.54	6.46	6.34	5.39	–	–
$Vol._{Ge(B)}$	5.28	5.31	5.59	7.28	–	–
Bridging angle‡	178.9(1)	179.1(1)	178.9(1)	176.9(1)	–	–

† 1NN = first nearest-neighbour, 3NN = third nearest-neighbour. ‡ Bridging angle determined under the assumption of only four Ge(*B*) bonds. BLD = $(100/n)\sum_{i=1}^{n}\{[|(X-O)_i - (\langle X-O\rangle)|]/(\langle X-O\rangle)\}\%$, n = amount of cation–anion bonds and X—O = cation–anion (oxygen) distance (Renner & Lehmann, 1986); ELD = $(100/n)\sum_{i=1}^{n}\{[|O-O)_i - (\langle O-O\rangle)|]/(\langle O-O\rangle)\}\%$, n = amount of edges and (O—O) = oxygen–oxygen interatomic distance defining an edge of the octahedron (Renner & Lehmann, 1986); OAV = $\sum_{i=1}^{12}(\Theta_i - 90°)^2/11$ with Θ_i = O—M—O bonding angle (Robinson *et al.*, 1971); TAV = $\sum_{i=1}^{6}\{(\Theta_i - 109.57°)^2/5$ with Θ_i = O—T—O bonding angle (Robinson *et al.*, 1971).

in the crystallographic *c* direction (Fig. 1*a*). *M*1-site chains and *M*2-site chains share two common corners and form a metal layer within the *bc* plane. Along *a*, these layers are separated by the GeO_4 tetrahedral chains (Fig. 1*b*). Two tetrahedral chains, with the basal plane of each tetrahedron facing each other (marked by arrows in Fig. 1*b*), are bound to each other per symmetry *via* a twofold axis. $CaMgGe_2O_6$ is closely related to the silicate mineral diopside, $CaMgSi_2O_6$, which can be seen as the *C*2/*c* parent structure type of the clinopyroxenes. A crystal chemical discussion of Ca-germanate clinopyroxene compounds, $CaM^{2+}Ge_2O_6$ (*M* = Mn, Co, Mg, Ni), will be given elsewhere (Redhammer *et al.*, 2005).

3.1. Structural topology of $CaCuGe_2O_6$ at 298 K

One of the main differences between 'normal' clinopyroxenes (*e.g.* $CaMgGe_2O_6$) and the title compound is observed for the Ge sites. While in the *C*2/*c* $CaMgGe_2O_6$ there is only one Ge^{4+} site, there are two different Ge positions, Ge(*A*) and Ge(*B*), in $CaCuGe_2O_6$. The Ge(*A*) cation is coordinated by four O atoms with Ge—O distances ranging between 1.708 (3) and 1.790 (3) Å, forming a distorted tetrahedron. The average Ge(*A*)—O bond length is 1.754 (3) Å, which is similar to the value in $CaMgGe_2O_6$ of 1.755 (2) Å. With respect to the bond- and edge-length distortion parameters (BLD and ELD, respectively; Renner & Lehmann, 1986), the Ge(*A*) tetra-

hedron in the title compound is comparable to the tetrahedral site in $CaMgGe_2O_6$. The parameters are BLD = 1.89% (2.38%) and ELD = 1.89% (2.73%) in $CaCuGe_2O_6$ ($CaMgGe_2O_6$). The O—Ge—O bond angles range between 103.0 (1) and 120.5 (1)°, reflecting a large quadratic tetrahedral angle variance (TAV; Robinson *et al.*, 1971) of 38.29°. The τ angle, which defines the average O—Ge—O bond length from the 'base' of the tetrahedron to the apex O atom, is 112.9 (1)°. Thus, the Ge(*A*) tetrahedron appears to be elongated in the *a* direction. The GeO_4 tetrahedron in the Mg^{2+} analogue is also stretched along the *a* axis [τ = 114.64 (9)°] and exhibits an even larger quadratic TAV of 51.67°. Individual tetrahedra are connected to each other *via* the O3*A* atoms to form infinite chains along **c** (Fig. 2*a*). These chains are distinctly kinked, which is expressed by the small tetrahedral bridging angle O3*A*—O3*A*—O3*A* 137.2 (1)° and marked as a bold white bond in Fig. 2(*a*). A fully extended chain would have a bridging angle of 180°; that in $CaMgGe_2O_6$ is 159.76 (8)°.

While in the *C*2/*c* clinopyroxenes the GeO_4 chains are identical from layer to layer along *a* (Fig. 1*b*), $CaCuGe_2O_6$ is characterized by a strong distortion of every alternate layer (Ge*B* sites, Fig. 2*b*). The twofold axis, constraining two

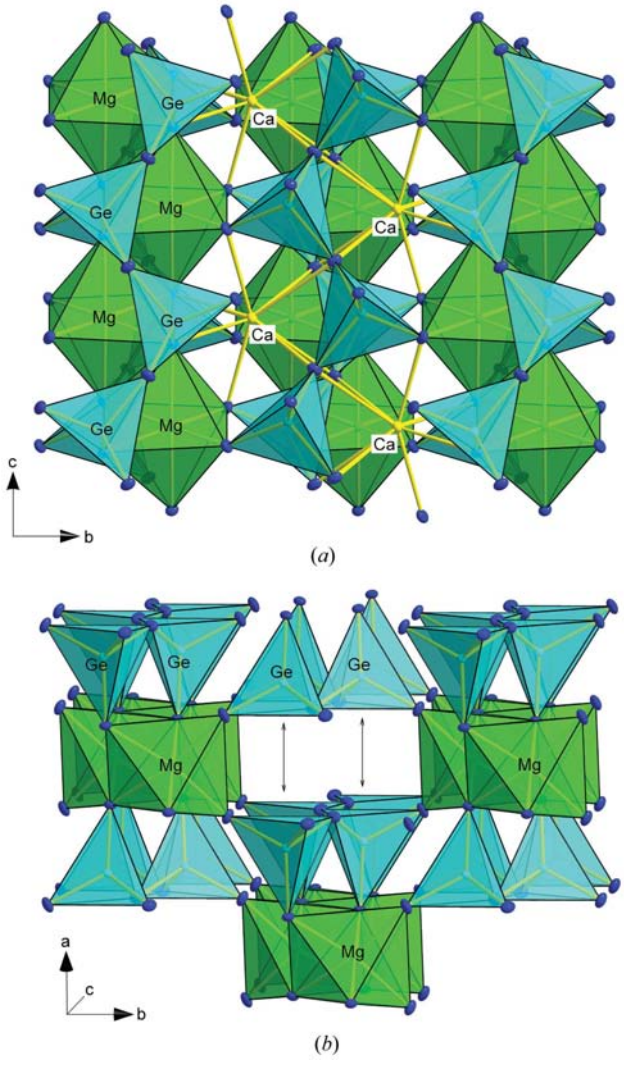

Figure 1
Structure of $CaMgGe_2O_6$ clinopyroxene-type germanate at 298 KP: (*a*) viewed along [100] and (*b*) in a three-dimensional display.

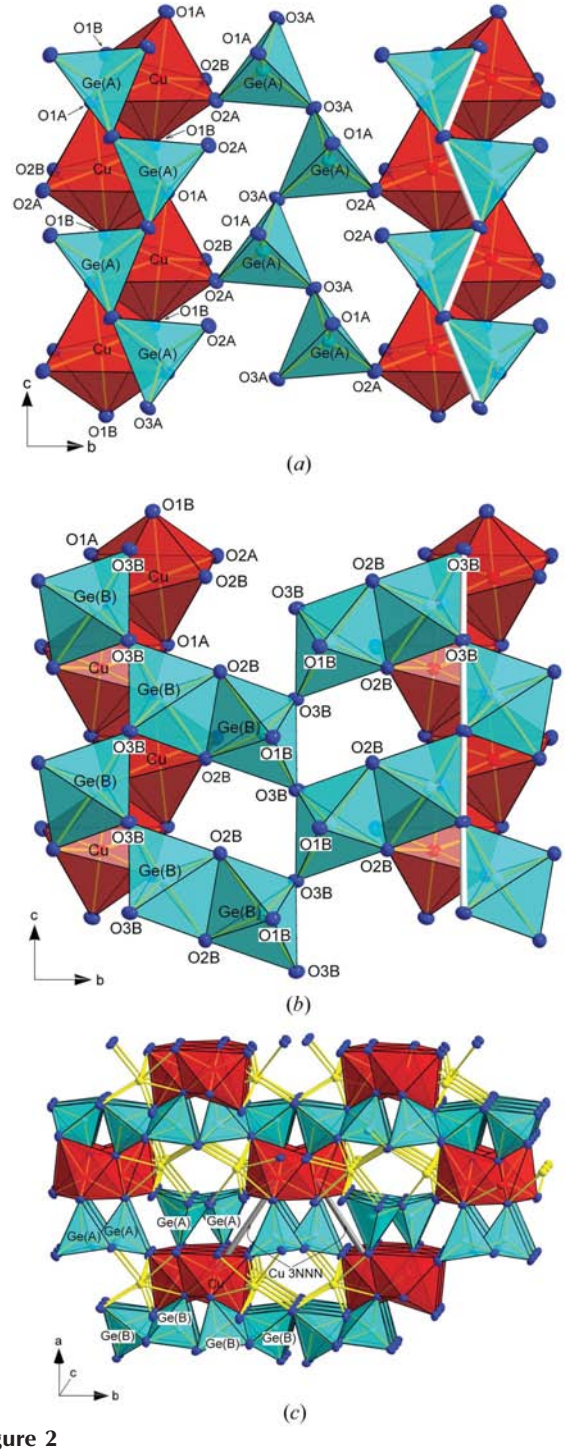

Figure 2
Section of the structure of $CaCuGe_2O_6$ at 298 K: (*a*) viewed along [100] showing the layer of Ge(*A*)O_4 tetrahedra (*A* layer) and (*b*) the layer of Ge(*B*)O_5 bipyramids. The view in (*c*) depicts the three-dimensional structure of $CaCuGe_2O_6$.

tetrahedral chains in different layers to be symmetrically equivalent (Figs. 1*a* and *b*), is missing here. The Ge*B* site is fivefold coordinated with three Ge—O distances between 1.764 (3) and 1.774 (3) Å, the fourth one being 1.892 (3) Å. The O2*B* atom is 2.080 (4) Å away from Ge*B*, but is considered to be bonded on the basis of bond-strength calculations (bond strengths S_i = 0.41 v.u.; Brese & O'Keeffe, 1991). Thus, the Ge*B* site forms a trigonal bipyramid with an average Ge—O distance of 1.856 (3) Å. Individual GeO_5 bipyramids are connected to each other by a common edge (O2*B*—O2*B*), thereby forming a true two-dimensionally connected layer (*B* layer). The length of this common edge is 2.529 (4) Å, which is distinctly shorter than the corresponding O2*A*—O2*B* distance of 3.558 (4) Å in the *A* layer. It is this extreme shortening of the O2*B*—O2*B* interatomic distance which brings the O2*B* atom into the coordination sphere of Ge*B*. The GeO_5 bipyramid is characterized by an elongation in the *a* direction. The bond- and edge-length distortion parameters are large, with BLD = 5.59% and ELD = 7.25%, respectively. Taking into account only the four shorter Ge—O distances, straight one-dimensional tetrahedral chains are formed with a tetrahedral bridging angle of 178.9 (1)° (bold bonds in Fig. 2*b*). However, this tetrahedron is extremely distorted with an average O—Ge—O bond angle of 106.6 (1)° and a quadratic TAV of 250.50°.

The *M*1 cation Cu^{2+} is coordinated by six O atoms, forming a strongly deformed octahedron with four shorter and two longer Cu—O bond lengths (Table 2). This is consistent with a tendency of the Cu^{2+} cation to form Jahn—Teller distorted CuO_4O_2 octahedra. Three Cu—O bond lengths are within 1.939 (4) and 1.968 (4) Å, and compare well with Cu—O bond lengths in other copper germanate compounds such as $CuGeO_3$ [1.934 (2) Å; Braden *et al.*, 1999] or $Cu_2Sc_2Ge_4O_{13}$ [2.931 (3)–2.011 (3) Å; Redhammer & Roth, 2004*c*]. In all these compounds Cu^{2+} exhibits a fourfold planar coordination, which is regarded as occurring more frequently than the sixfold (4 + 2) coordination found here. The two long bonds in $CaCuGe_2O_6$ lie within the equatorial plane of the octahedron and the CuO_6 octahedron appears to be distinctly compressed along the *c* direction. This strong deviation of the Cu^{2+} site from an ideal octahedral geometry is expressed by the distortion parameters with BLD = 7.93%, ELD = 8.35% and quadratic OAV = 96.0°. In $CaMgGe_2O_6$ the *M*1 octahedra are comparably regular (BLD = 1.34%, ELD = 3.39%, quadratic OAV = 31.69°). It is mainly the elongation of the Cu—O1*A* and the Cu—O2*B* bond lengths which causes the large polyhedral distortion. The elongation of the Cu—O2*B* bond is also responsible for the shift of the fifth O atom into the coordination sphere of the GeO_5 bipyramid. Fig. 3 is a direct comparison of the *M*1 site in $CaCuGe_2O_6$ and $CaMgSi_2O_6$ at 298 K.

It is interesting to note that within the *M*1 chain the shortest *M*1—*M*1 interatomic distance (1NN = first nearest-neighbour) is distinctly shorter [3.072 (2) Å] in $CaCuGe_2O_6$ than that in $CaMgGe_2O_6$ [3.147 (1) Å], although Cu^{2+} is the slightly larger cation. However, the Cu—Cu interatomic distance is large in $CaCuGe_2O_6$ compared with other Cu-bearing germanate compounds such as $CuGeO_3$ [edge-sharing chains of CuO_4 plaquets, Cu—Cu 1.943 (1) Å; Braden *et al.*, 1999], $SrCu_2(BO_3)_2$ [Cu_2O_6 dimers, Cu—Cu 2.903 (2) Å; Sparta *et al.*, 2001] or $Cu_2Sc_2Ge_4O_{13}$ [Cu_2O_6 dimers, Cu—Cu 3.011 (4) Å; Redhammer & Roth, 2004*c*]. It is the incorporation of Cu^{2+} into the *M*1 chain and the strong bond connection of the *M*1 chain with the chains of GeO_4 tetrahedra and layers of GeO_5 bipyramids which obviously lengthens the interatomic Cu—Cu distance within the *M*1 chain. The second shortest Cu—Cu interatomic distance (2NN, second nearest-neighbour) is also within the *M*1 chain and amounts to 5.208 (2) Å, whereas the 3NN (third nearest-neighbour) Cu—Cu distance is between neighbouring *M*1 chains (Fig. 2*c*).

Besides the distortion of every second Ge layer resulting in the formation of the GeO_5 bipyramids and the strong Jahn–Teller distortion of the *M*1 octahedra, there is another difference between 'normal' *C*2/*c* clinopyroxenes and the title compound. This concerns the Ca^{2+} site, which is in an irregular sevenfold coordination with Ca—O distances ranging between 2.441 (2) and 2.627 (2) Å. Owing to the distinct kinking of the Ge(*A*) tetrahedral chain, one of the O3*A* bridging O atoms is removed from the coordination of Ca^{2+} [Ca—O3*A* 3.332 (4) Å]. In the *C*2/*c* $CaMgGe_2O_6$, Ca^{2+} is eightfold coordinated with Ca—O distances ranging between 2.373 (2) and 2.648 (2) Å. The average Ca—O bond length is of similar size with 2.474 (4) and 2.508 (3) Å for the Cu^{2+} and Mg^{2+} compounds, respectively. In both compounds Ca^{2+} fills up the interstitial space between octahedral *M*1 and tetrahedral GeO_4 chains and GeO_5 layers (Fig. 2*c*).

3.2. Magnetic measurements

Magnetic measurements were used as an additional characterization method. Fig. 4(*a*) shows the magnetic susceptibility $\chi(T)$ of $CaCuGe_2O_6$ at an applied field of 1 Tesla in the field cooling process between 2 and 300 K. The most prominent characteristic is that the susceptibility shows a distinct, broad maximum at 40 K but drops rapidly toward 0 for $T <$ 40 K. According to Sasago *et al.* (1995) the experimental

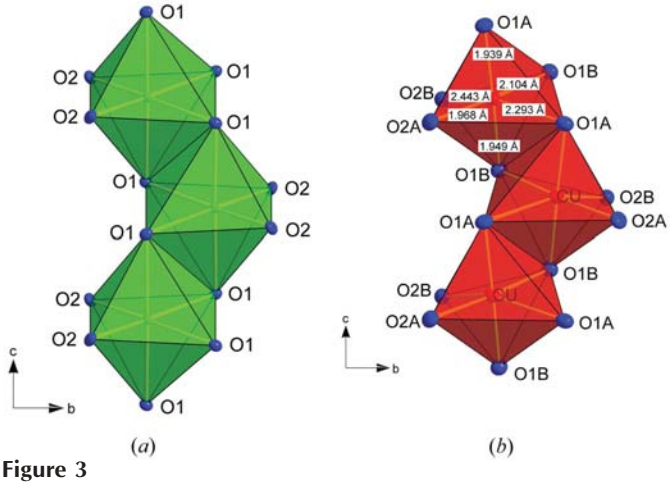

Figure 3
Comparison of octahedral *M*1 site geometry in $CaMgGe_2O_6$ and $CaCuGe_2O_6$ at 298 K.

results reveal that the ground state is a spin singlet and that there is a finite energy gap between the ground and the excited states. However, the broad maximum around 40 K is a characteristic feature of low-dimensional antiferromagnetic spin systems. Thus, below 40 K the presence of antiferromagnetically coupled Cu^{2+} dimers is assumed. The dimers are assigned to the third nearest-neighbour Cu pairs (Sasago *et al.*, 1995; Valenti *et al.*, 2002). Furthermore, the inter-dimer interaction is assumed to be ferromagnetic. At very low temperatures, $\chi(T)$ again increases. This was interpreted by Sasago *et al.* (1995) as being due to magnetic impurities and/or defects at the Cu^{2+} site. According to the simple model of Sasago *et al.* (1995) to remove the low-temperature 'impurity' we calculate $\chi_t(T) = \chi(T) - C/T$ with $C = 0.022$ emu K mol^{-1} (Fig. 4*a*).

If we apply a Curie–Weiss law (CW) in the temperature range 200–330 K we find the following values C_{CW} = 0.5105 emu K mol^{-1}, $\mu_{CW} = 2.02\ (2)\mu_B$ and $\theta_p = -34.7\ (3)$ K for $\chi(T)$ in an external field of $H = 1$ T. The negative paramagnetic Curie temperature θ_p suggests antiferromagnetic coupling at $T < 40$ K, in agreement with the findings of Zheludev *et al.* (1996). Below 150 K a deviation from the paramagnetic state is observable. The results are shown in Fig. 4(*a*). Furthermore, we compare $\chi_t(T)$ with the theoretical susceptibility of isolated AF dimers, $\chi_d(T)$, with $g = 2.07$ and $J/k_B = -34$ K proposed by Sasago *et al.* (1995); see Fig. 4(*b*). For the synthesized polycrystalline material $CaCuGe_2O_6$, we found the characteristic features. Valenti *et al.* (2002) pointed out that the dimers are formed by 3NN magnetic Cu^{2+} ions ($S = \frac{1}{2}$) with ferromagnetic inter-dimer couplings *via* 1NN. The best parameters of both interactions are $J_3/k_B = -67$ K and $J_1 = -0.2\,J_3$.

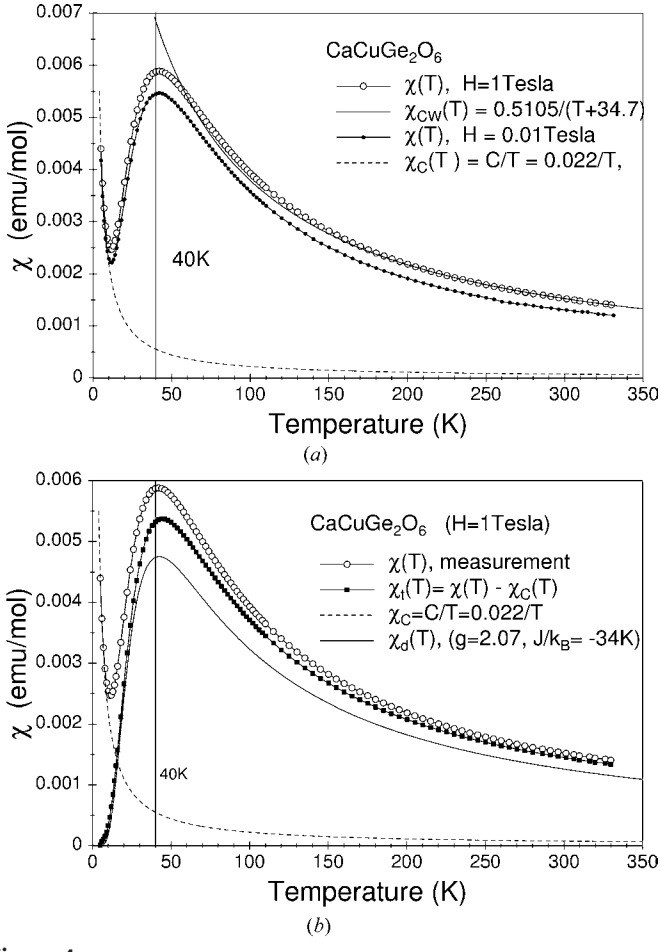

Figure 4
Magnetization of $CaCuGe_2O_6$ as a function of temperature. (*a*) The temperature dependence of the magnetic susceptibility $\chi(T)$ of $CaCuGe_2O_6$ measured in external magnetic fields $H = 1$ Tesla (open circles) and 0.01 Tesla (solid circles). The solid curve represents the Curie–Weiss fit $\chi_{CW}(T) = 0.5105/(T + 34.7)$ and the dashed curve $\chi_C(T) = 0.022/T$. (*b*) The magnetic susceptibility $\chi(T)$ of $CaCuGe_2O_6$ as measured in an external magnetic field $H = 1$ Tesla (open circles); the difference, $\chi_t(T) = \chi(T) - \chi_C(T)$, is shown as solid squares and the theoretical calculation for isolated AF dimers $\chi_d(T)$ with the parameters $g = 2.07$ and $J/k_B = -34$ K is drawn as a solid curve.

3.3. Structural variations with temperature

3.3.1. Unit-cell parameters. The unit-cell parameters do not vary linearly with temperature, but exhibit two different events, one at *ca* 40 K and one at 655 K (Fig. 5). There are no extra reflections or splitting of Bragg reflections below 40 K and $CaCuGe_2O_6$ retains $P2_1/c$ symmetry. The low-temperature event (insets in Fig. 5) would then have to be solely attributed to the magnetic phase transition taking place at 40 K. It is characterized by small discrepancies in all the lattice parameters due to magneto-striction of the lattice. The interaction path between the third next-nearest-neighbour Cu pairs (to which the formation of Cu dimers is attributed) is primarily aligned within the *ab* plane and has only a small displacement along the *c* direction. Thus, any magneto-striction effects of the lattice should mainly affect the *a* and *b* lattice parameters. Indeed, a distinct shortening is found for *a* with a somewhat less pronounced one for *b*, which is consistent with the expectation from the magnetic ordering scheme. As the *c* lattice parameter is also somewhat shortened after the magnetic phase transition, it may be argued that there is an additional coupling of Cu^{2+} ions within the *M*1 chain, which runs parallel to the *c* axis. However, on the basis of our data we cannot exclude the possibility that there is also a crystallographic phase transition at which the monoclinic cell transforms to a triclinic one. Superstructure reflections might be too weak to be detected with powder X-ray diffraction and the metric change would have to be so small that it would not be detected, given the resolution of our powder diffraction measurements (full width at half-maximum, FWHM, of *ca* 0.08° at 45° 2θ). The formation of Cu–Cu pairs within the *M*1 chain would only be possible for a triclinic cell. For $NaTiSi_2O_6$ the magnetic phase transition at *ca* 200 K is accompanied by a crystallographic phase transition from $C2/c$ to $P\bar{1}$, which allows the formation of a Ti–Ti pair within the *M*1 chain (Redhammer *et al.*, 2003).

Between 40 and 650 K there is a continuous, slightly non-linear increase of lattice parameters. Small changes in the gradient of a plot of data points as a function of temperature take place at 550 K, but no change in symmetry occurs. Between 650 and 670 K the lattice parameters *a* and *c*, the

monoclinic angle β and the unit-cell volume increase by 0.20, 2.89, 1.01 and 1.64%, respectively, whereas b decreases by 0.86%. Above 670 K the powder diffraction diagrams reveal $C2/c$ symmetry. The changes in unit-cell parameters are distinctly larger than those found by Redhammer & Roth (2004*b*) for $P2_1/c$ to $C2/c$ phase transitions in lithium silicate clinopyroxenes. Furthermore, the phase transitions in the lithium pyroxenes are rapid and pyroxenes occur within a very narrow temperature window. In $CuCuGe_2O_6$, however, a broad region of 30 K exists, in which both phases are present. It was not possible here to deduce the lattice parameters with any accuracy so no reliable temperature variations could be obtained (not included in Fig. 5). However, there is a distinct hysteresis behaviour and within the two-phase region the phases seem to stabilize each other.

Within the $P2_1/c$ phase of $CaCuGe_2O_6$, the thermal expansion is largest for the c unit-cell parameter. From the data available (298–600 K), linear thermal expansion coefficients (α) have been calculated with $\alpha = 7.2\,(3) \times 10^{-6}$, $14.6\,(3) \times 10^{-6}$ and $20.3\,(3) \times 10^{-6}\,K^{-1}$ for a, b and c, respectively. For the $C2/c$ phase, the thermal expansion is similar except in the c direction [$\alpha = 6.6\,(3) \times 10^{-6}$, $16.6\,(3) \times 10^{-6}$ and $8.3\,(3) \times 10^{-6}\,K^{-1}$ for a, b and c, respectively].

3.3.2. The octahedral *M*1 site. Increasing the temperature increases the average Cu—O bond lengths within the $P2_1/c$ phase (Fig. 6*a*). Among the six independent Cu—O bond lengths, the three short Cu—O distances show the smallest variations with temperature (Fig. 6*b*), whereas the Cu—O1*A* and Cu—O1*B* distances, which are within the equatorial plane of the octahedron, increase significantly with temperature (Figs. 6*c* and *d*). These O1*A* and O1*B* atoms form an edge, which is common to the *M*1 and *M*2 (CaO_7) sites, respectively. Furthermore, each one of the two O atoms is a corner of the common edge between neighbouring *M*1 sites. The increase in Cu—O1*A* and Cu—O1*B* bond lengths directly correlates with the distinct increase by $\simeq 1.5\%$ of the shortest Cu—Cu interatomic distance (Fig. 6*e*). The two common edges between neighbouring *M*1 sites (O1*A*—O1*B* edges going from the equatorial plane of the octahedron to the apex O atom, respectively) do not show a length variation with temperature, whereas the O1*A*—O1*B* edge, which is within the equatorial plane of the octahedron, increases and accounts for the increase in Cu—Cu (1NN) with temperature. The second shortest Cu—Cu distance (2NN) is also within the *M*1 chain (parallel to the c direction) and also increases with temperature. The third shortest Cu—Cu distance (3NN) is found between two neighbouring *M*1 chains, separated by a sheet of

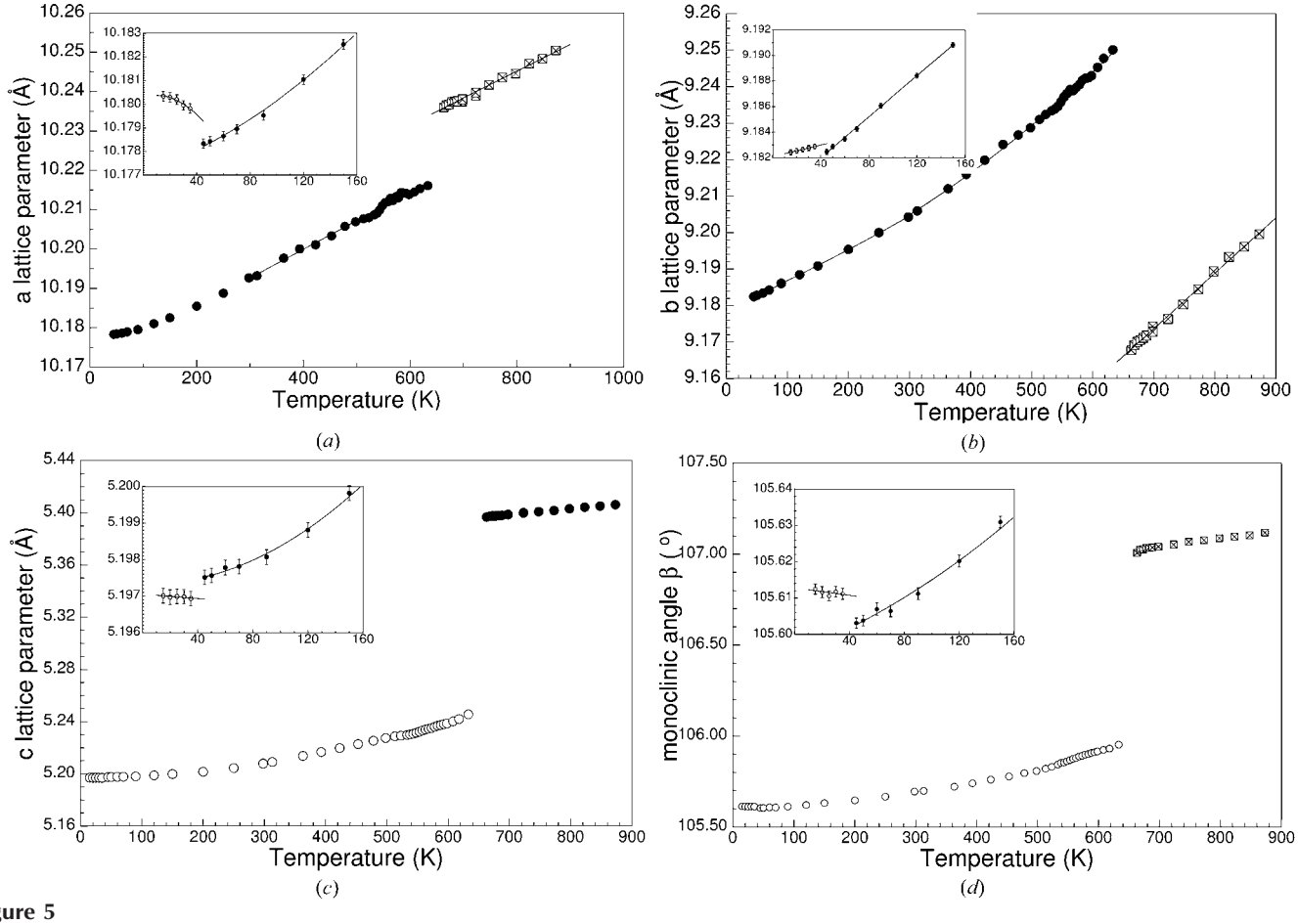

Figure 5
Lattice parameters of $CaCuGe_2O_6$ as a function of temperature; the insets show the low-temperature regions. Error bars are smaller than the symbols if not visible.

GeO_4 tetrahedral chains along *a*. It is the interaction path between these 3NN Cu—Cu pairs which is proposed to be mainly responsible for the magnetic properties of the title compound. As temperature is increased, this 3NN Cu—Cu distance increases. The increase becomes more prominent when the phase transition temperature is approached (Fig. 6*f*). It is interesting to note that the 4NN Cu—Cu distance distinctly decreases with increasing temperature within the $P2_1/c$ phase. The changes in 3NN and 4NN Cu interatomic distances correlate well with the alterations of the kinking state of the tetrahedral chains in the vicinity of the phase transition (see below). With respect to the distortion parameters BLD and ELD, no systematic temperature variations can be deduced from the data. However, the quadratic OAV decreases significantly with increasing temperature by *ca* 16% between 100 and 650 K. Generally, all bond angles approach

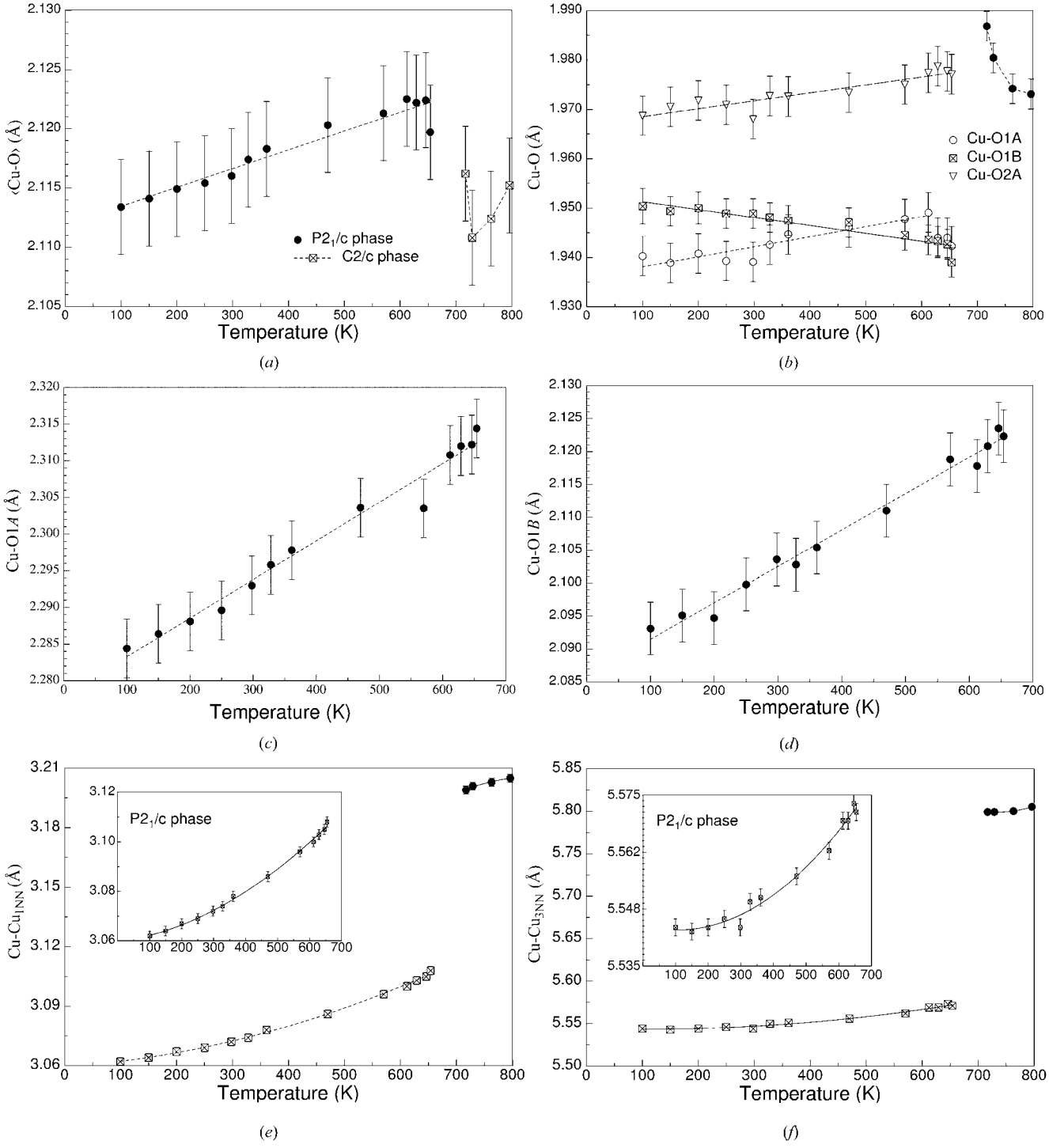

Figure 6
Variation of structural parameters of the CuO_6 (*M*1) site with temperature. (*a*) average Cu—O bond length; (*b*)–(*d*) individual Cu—O bond lengths; (*e*) first nearest-neighbour Cu—Cu interatomic distance; (*f*) third nearest-neighbour Cu—Cu interatomic distance.

the ideal value of 90° upon heating (even if they still depart significantly from it at 650 K). The most prominent angles are O1*A*—Cu—O2*A*, which decreases by 2.5%, and O1*B*—Cu—O2*B*, which increases by 1.8%. Both angles are within the equatorial plane of the octahedron and correlate well with the decrease of the O1*A*—O2*A* edge length by 0.9% and the increase of the O1*B*—O2*B* edge by 1.9%. Both edges are among the ones showing the largest alterations with temperature.

The phase transition from the LT-$P2_1/c$ to the HT-$C2/c$ structure is accompanied by distinct bond-length changes. Within the $C2/c$ phase the CuO_6 octahedron is stretched along **c** with the average Cu—O_{apex} bond lengths (Cu—O1*A*, CuO1*B* in $P2_1/c$, Cu—O1 in $C2/c$) increasing by $\simeq 0.04$ Å when changing from the LT to the HT form (Fig. 6*b*). The octahedron, however, still remains tetragonally compressed. In $C2/c$ the Cu—O1 bonds, which lie within the equatorial plane of the octahedron, are only slightly larger than the average of the corresponding Cu—O1*A* and Cu—O1*B* bonds in $P2_1/c$. Pronounced changes, however, occur for the Cu—O2 bonds at the phase transition. The long Cu—O2*B* bond becomes shortened by as much as 13% and the Cu—O2*A* bond is stretched by 6.5% during the phase transition. The movement of the O2*B* atom towards Cu^{2+} removes this O atom from the coordination sphere of Ge(*B*). These large bond-length changes are mainly due to the changes in the kinking state of the tetrahedral chains, connected to the octahedral chains *via* the O2*A* and O2*B* atoms by corner sharing. While in $P2_1/c$ the four shorter Cu—O bonds define a common plane perpendicular to the equatorial plane of the octahedron, they do not in $C2/c$. The movement of the O2 atoms brings them closer to the Cu atom compared with the equatorial O1 atoms. Therefore, the longest Cu—O distances in $C2/c$ are those involving O1 atoms, which form a common edge between the *M*1 and *M*2 sites. Increased repulsive forces possibly become active as Ca^{2+} and Cu^{2+} approach each other; Cu^{2+} is then displaced out of the centre of the octahedron. The interatomic distances between neighbouring Cu atoms also change at the phase transition. The Cu—1NN distances increase by nearly 0.1 Å, whereas the Cu—3NN distances decrease by 0.37 Å (Figs 6*e*–*f*). It is mainly the altered conformational state of the tetrahedral chain which is responsible for these distinct changes.

In general, the CuO_6 octahedron is much more regular in the $C2/c$ phase. All the parameters (BLD, ELD and OAV) are smaller by more than 50%. Thus, in $C2/c$ Cu^{2+} occupies a more regular octahedron, which – in terms of distortion parameters – is comparable with *e.g.* the $Fe^{3+}O_6$ octahedron in $NaFeSi_2O_6$, well known under the mineral name aegirine (BLD = 2.98%, ELD = 3.19%, OAV = 55.3°; Redhammer & Roth, 2002). While in $P2_1/c$ a 4+2 coordination to Cu^{2+} may be assigned, it is a true sixfold octahedral coordination in $C2/c$. However, the *M*1 site (CuO_6 site) in $C2/c$ is still more distorted than the *M*1 site, *e.g.* in $C2/c$ $CaMgGe_2O_6$.

3.3.3. The GeO_4 and GeO_5 sites. In silicate and germanate compounds tetrahedra generally behave as rigid units if a parameter of state such as the temperature is changed. This also holds true for $CuCuGe_2O_6$. There are only minor changes in bond lengths within the $P2_1/c$ phase at the Ge(*A*)O_4 site. The average Ge—O bond length stays constant, both within and between the $C2/c$ and $P2_1/c$ phases. A small variation with temperature is detectable only for the Ge(*A*)—O3 bond length (Fig. 7*a*). At the phase transition, Ge(*A*)—O1*A* and Ge(*A*)—O2*A* remain almost constant, whereas for Ge—O3*A* and Ge(*A*)—O3*B* some more significant changes appear. The edge lengths also remain quite constant within the $P2_1/c$ phase; however, there are several distinct changes at the phase transition which are due to changes in bond angles between the $P2_1/c$ and the $C2/c$ phase. Both O1—Cu—O3 angles in $C2/c$ are larger by *ca* 3.5° compared with the corresponding ones in $P2_1/c$, whereas the O1—Cu—O2 angle decreases by *ca* 3°. All these three are angles from the O1 apex to the basal plane O atoms of the tetrahedron and define the τ angle (which is the average). τ is larger by *ca* 1° in $C2/c$ and, consequently, the tetrahedron appears to be more elongated along *a* compared with the $P2_1/c$ phase. Except for the O1*A*—Ge—O2(*A*) angle, all other bond angles successively depart more and more from the ideal tetrahedral angle of 109.47° with increasing temperature; consequently, the quadratic tetrahedral angle variance (TAV) is larger for the $C2/c$ phase.

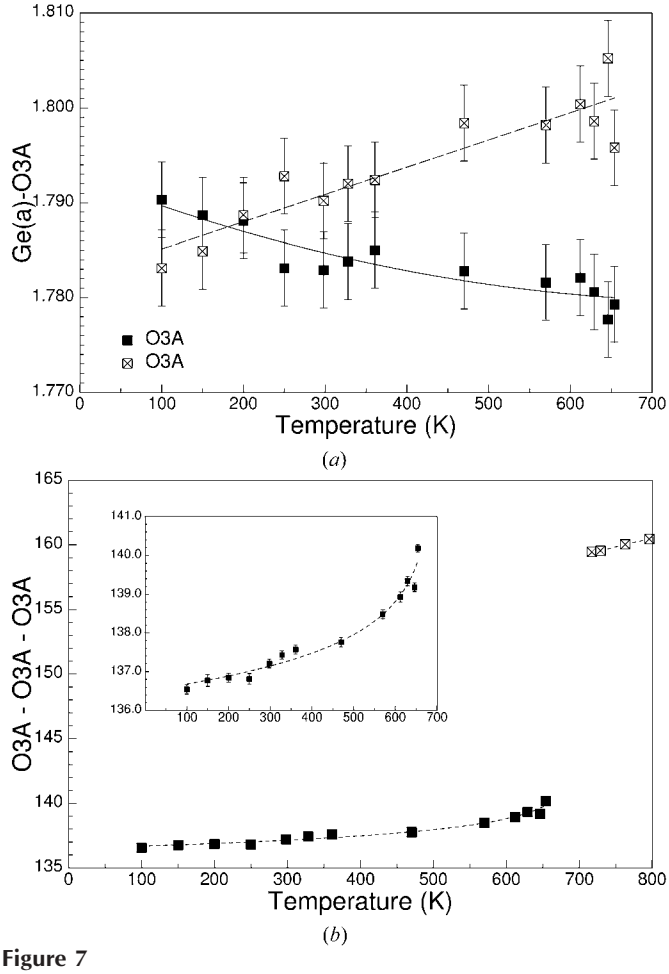

Figure 7
Variation of structural parameters of the Ge(*A*)O_4 tetrahedral site with temperature. (*a*) Selected individual Ge(*A*)—O bond lengths and (*b*) tetrahedral bridging angle O3*A*—O3*A*—O3*A*.

Among all the structural alterations, which occur at the Ge(A)O_4 site, the most important is the change in kinking state of the tetrahedral chains. As noted in §3.1, the tetrahedral chains deviate strongly from a linear chain. At 100 K the O3A—O3A—O3A angle is 136.5 (1)°. Increasing the temperature causes a non-linear increase up to 140.2 (1)° close to the phase transition (Fig. 7*b*). At the phase transition the two Ge sites in $P2_1/c$ become identical and the kinking of the tetrahedral chain decreases to 159.4 (1)°. A further increase of temperature also increases the O3—O3—O3 angle, *i.e.* decreases the kinking state and stretches the tetrahedral chain along the *c* direction. As a consequence, the M1 chains are brought closer together and the lateral dimension along *b* is reduced.

At the Ge(B)O_5 site, bond lengths change more distinctly with temperature. Even if the changes are within three times the standard deviation it can be concluded that all of the four shorter Ge(B)—O bond lengths tend to decrease with increasing temperature (Figs. 8*a* and *b*) and approach the smaller Ge—O bond lengths found in $C2/c$. The Ge(B)—O3A bond length, however, becomes successively longer with increasing temperature (Fig. 8*c*) and is finally removed from the coordination sphere of Ge(B). The distinct increase of Ge(B)—O3B is due to the movement of the O3B atom towards Cu^{2+}, as mentioned previously. The O3B—O3B—O3B angle, which would correspond to the kinking angle if the fifth coordinating oxygen were removed, tends to firstly increase but then decreases with increasing temperature. This behaviour is one of several signs that with increasing temperature the $P2_1/c$ structure becomes unstable and approaches $C2/c$ symmetry.

3.3.4. The *M*2 site. Except Ca—O1A, all the Ca—O bond lengths increase with increasing temperature (Figs. 9*a–c*) within the $P2_1/c$ phase. At the phase transition Ca^{2+} is moved closer to the M1 chain as the Ca—O1 and Ca—O2 bond lengths in $C2/c$ [2.405 (4) and 2.363 (4) Å, respectively] are shorter than the average of the corresponding bond lengths in $P2_1/c$ [2.462 (4) and 2.434 (4) Å, respectively]. On the other hand, and as a consequence of the changes in the tetrahedral kinking angle at the phase transition, the O3 atoms are further away from Ca^{2+} in $C2/c$. However, a fourth O3 atom is brought into the coordination sphere of Ca^{2+}, which thus becomes eightfold coordinated.

Among all the polyhedra, the M2—O polyhedra are most sensitive to temperature changes. This is readily seen when comparing the relative changes in the coordination polyhedra volumes in $CaCuGe_2O_6$ within the $P2_1/c$ phase (Fig. 10). The volume increase of the CuO_6 octahedron is smaller than that of the M2 site, but distinctly larger than that of the tetrahedrally coordinated Ge(A) site which shows practically no volume expansion with temperature. The fivefold coordinated Ge(B) site is intermediate between the Ge(A) and the M1 site. As the tetrahedra are connected to the M1 octahedra *via* common corners an effective mechanism has to be active, which accounts for the different thermal expansions of these structural units. This mechanism can be found in the variations of the tetrahedral bridging angle. By decreasing the kinking (increasing the O3—O3—O3 angle), the tetrahedral chain is stretched and can match the M1 site chain.

4. Conclusions

(i) $CaCuGe_2O_6$ represents one of the most distorted clinopyroxene structures known so far. This distortion is due

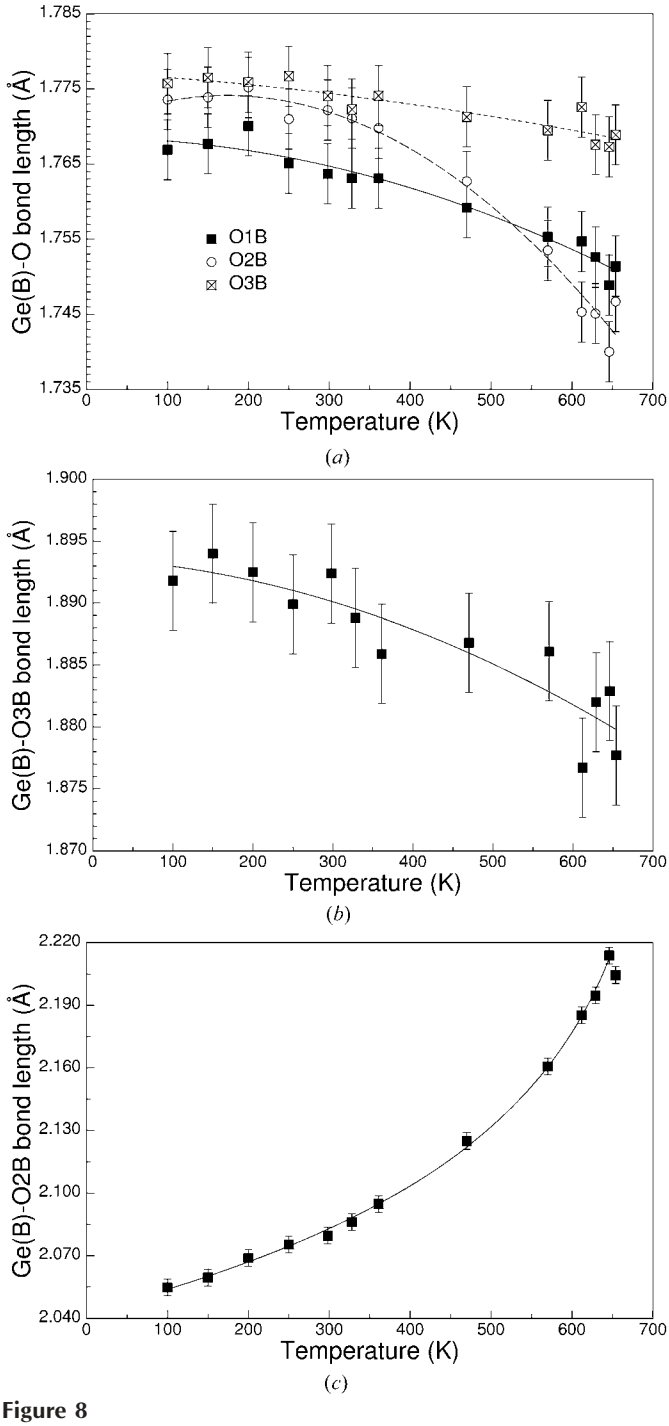

Figure 8
Variation of structural parameters of the Ge(B)O_5 bipyramidal site with temperature: (*a*)–(*c*) individual Ge(B)—O bond lengths. Lines are low-order polynomials and are intended as guides to the eye.

to the specific nature of the Cu^{2+} cation with its tendency to form Jahn–Teller distorted CuO_4O_2 octahedra. This behaviour results in a strong distortion of the *M*1 octahedron and a distortion of every second Ge-site layer, with the formation of a true two-dimensionally connected layer of GeO_5 bipyramids rather than layers consisting of one-dimensionally connected GeO_4 tetrahedral chains. Similar to the $P2_1/c$ lithium clinopyroxenes, the coordination number of the *M*2 site cation is reduced compared with the corresponding *C*2/*c* symmetry, *e.g.* sevenfold-coordinated Ca^{2+} in $P2_1/c$ $CaCuGe_2O_6$, eightfold-coordinated Ca^{2+} in *C*2/*c* $CaMgGe_2O_6$.

(ii) The large thermal expansion along **c** can be directly correlated with the 1NN and 2NN Cu—Cu distances and the O3—O3—O3 angle variations. At the phase transition the sharp increase in *c* is due to the stretching of the tetrahedral chains which, in turn, also causes a contraction along **b**. As in other clinopyroxenes showing a transition from the LT $P2_1/c$ to HT *C*2/*c*, the changes in lattice parameters are largely controlled by the kinking state of the tetrahedral chain.

(iii) $CaCuGe_2O_6$ represents one of the rare cases in which Cu^{2+} is sixfold coordinated and forms octahedral chains with antiferro-distortive Cu^{2+} ions. Within the $P2_1/c$ phase the oxygen coordination is still very distorted, which may be described by a 4 + 2-fold coordination, more frequently found for Cu^{2+}. In the HT *C*2/*c* a true octahedral configuration around Cu^{2+} is formed. The polyhedral distortion of the $Cu^{2+}O_6$ octahedron is comparable to that of the $Fe^{3+}O_6$ octahedra found in *e.g.* the clinopyroxene compounds $NaFe^{3+}Si_2O_6$ and $LiFe^{3+}Si_2O_6$ (Redhammer & Roth, 2002).

(iv) The proposed, almost complete compensation of first- and second-next-nearest interactions of Cu^{2+} cations needs to be re-evaluated and discussed based on these new data at the temperatures where the magnetic properties change. Extrapolation of structural data from ambient temperature is definitely not sufficient in such a structure-sensitive compound.

(v) Changes in lattice parameters at 40 K are ascribed to the magnetic phase transition due to a magneto-striction of the lattice. The shortening of especially the *a* and the *b* lattice parameters is assigned to the formation of Cu dimers, while the shortening of *c* may be assigned to the (anti)ferromagnetic coupling of these dimers within the *M*1 octahedral chain.

This work was supported by the Austrian Fonds zur Förderung der Wissenschaftlichen Forschung (FWF) under grant R33-N10 to G. J. Redhammer.

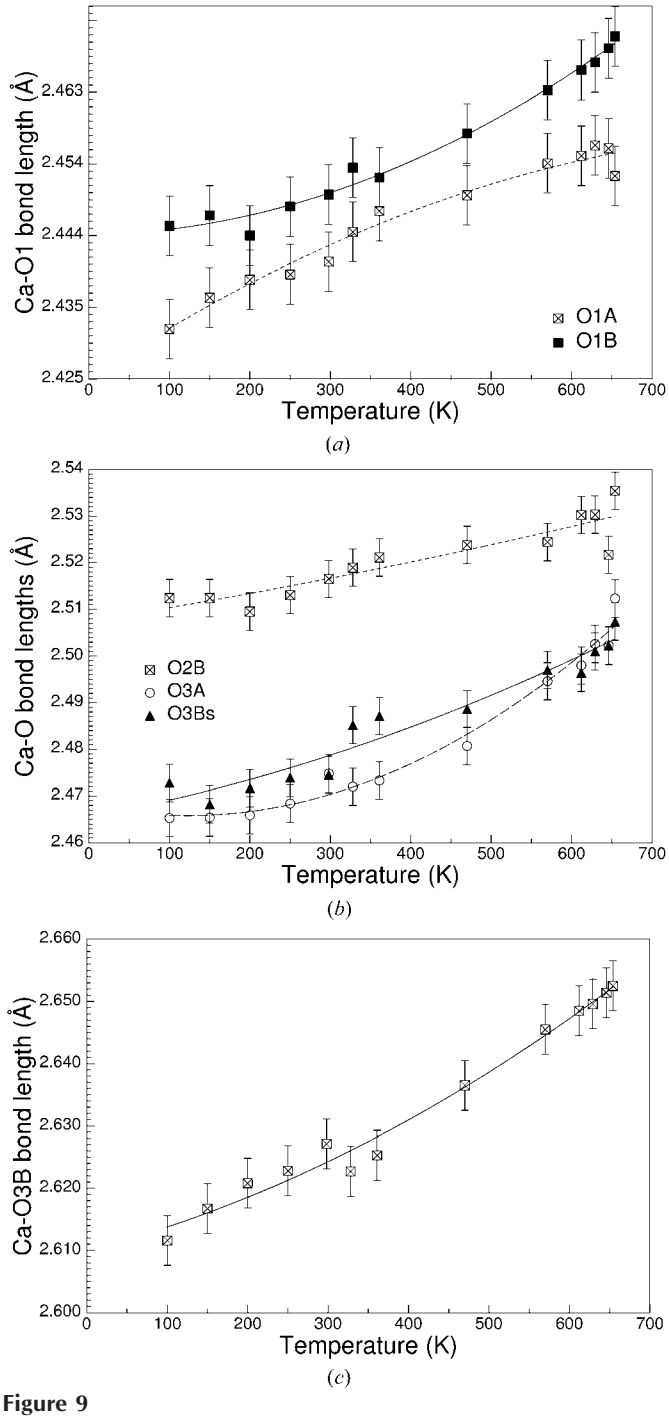

Figure 9
Variation of Ca—O bond lengths with temperature within the $P2_1/c$ phase for $CaCuGe_2O_6$.

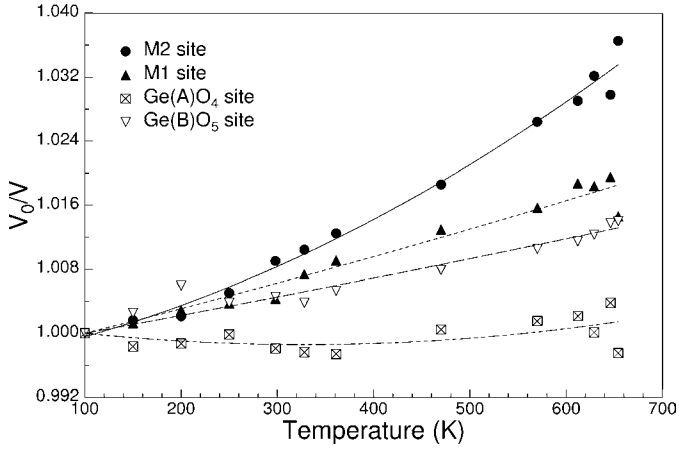

Figure 10
Relative changes of the polyhedral volumes of the coordination polyhedra in $CuCuGe_2O_6$ as a function of temperature within the $P2_1/c$ phase.

References

Behruzi, M., Breuer, K.-H. & Eysl, W. (1986). *Z. Kristallogr.* **176**, 204–217.

Braden, M., Buechner, B., Klotz, S., Marshall, G. W., Behruzi, M. & Heger, G. (1999). *Phys. Rev. B*, **60**, 9616–9622.

Bradenburg, K. & Berndt, M. (1999). *DIAMOND*, Release 2.1b. Crystal Impact GbR, Bonn, Germany.

Brese, N. E. & O'Keeffe, M. (1991). *Acta Cryst.* B**47**, 192–197.

Farrugia, L. J. (1999). *J. Appl. Cryst.* **32**, 837–838.

Gavilano, J. L., Mushkolaj, S., Ott, H. R., Millet, P. & Mila, F. (2000). *Phys. Rev. Lett.* **85**, 409–412.

Isobe, M., Nimomiya, E., Vasil'ev, A. N. & Ueda, Y. (2002). *J. Phys. Soc. Jpn*, **71**, 1423–1426.

Lumdsen, M. D., Granroth, G. E., Mandrus, D., Nagler, S. E., Thoompson, J. R., Castellan, J. P. & Gaulin, B. D. (2000). *Phys. Rev. B*, **63**, R9244–R9247.

Redhammer, G. J. (2001). Habilitation Thesis, 420 pp (in German).

Redhammer, G. J., Ohashi, H. & Roth, G. (2003). *Acta Cryst.* B**59**, 730–746.

Redhammer, G. J. & Roth, G. (2002). *Z. Kristallogr.* **217**, 1–10.

Redhammer, G. J. & Roth, G. (2004*a*). *Z. Kristallogr.* **219**, 278–294.

Redhammer, G. J. & Roth, G. (2004*b*). *Z. Kristallogr.* **219**, 585–605.

Redhammer, G. J. & Roth, G. (2004*c*). *J. Solid State Chem.* **177**, 2714–2725.

Redhammer, G. J., Roth, G., Treutmann, W., Paulus, W. & André, G. (2005). In preparation.

Renner, B. & Lehmann, G. (1986). *Z. Kristallogr.* **175**, 43–59.

Robinson, K., Gibbs, G. V. & Ribbe, P.-H. (1971). *Science*, **172**, 567–570.

Rodriguez-Carvajal, J. (2001). *CPD Newsl.* **26**, 12–19.

Sasago, Y., Hase, K., Uchinokura, K., Tokunaga, M. & Miura, N. (1995). *Phys. Rev. B*, **52**, 3533–3537.

Shannon, R. D. & Prewitt, C. T. (1969). *Acta Cryst.* B**25**, 925–934.

Sheldrick, G. M. (1997*a*). *SHELXS*97. University of Göttingen. Germany.

Sheldrick, G. M. (1997*b*). *SHELXL*97. University of Göttingen. Germany.

Sparta, K., Rousell, P., Redhammer, G. J., Heger, G., Roth, G., Ionenescu, A., Lemmens, P., Güntherrodt, G., Kageyama, H., Onizuka, K. & Ueda, Y. (2001). *Eur. Phys. J. B*, **19**, 507–516.

Stoe & Cie (1996). *X-SHAPE* and *X-RED*. Stoe and Cie, Darmstadt, Germany.

Stoe & Cie (2002). *X-AREA*. Stoe and Cie, Darmstadt, Germany.

Tovar, M. & Eysel, W. (1999). 18th IUCr Congress, Glasgow, Abstr. P08.19.024, 557.

Valenti, W., Saha-Dasgupta, T. & Gros, C. (2002). *Phys. Rev. B*, **66**, 054426.

Vonlanthen, P., Tanaka, K. B. & Goto, A. (2002). *Phys. Rev. B*, **65**, Art. No. 214413.

Wilson, A. J. C. (1992). Editor. *International Tables for Crystallography*, Vol. C. Kluwer Academic Publishers, Dordrecht, The Netherlands.

Zheludev, A., Shirane, G., Sasago, Y., Hase, M. & Uchinokura, K. (1996). *Phys. Rev. B*, **53**, 11642–11646.